J Nanopart Res (2013) 15:1667
DOI 10.1007/s11051-013-1667-5

RESEARCH PAPER

Sb_2O_3 microrods: self-assembly phenomena, luminescence and phase transition

Teresa Cebriano · Bianchi Méndez · Javier Piqueras

Received: 8 February 2013 / Accepted: 16 April 2013 / Published online: 25 April 2013

Abstract Sb_2O_3 microrods of the orthorhombic phase have been grown by evaporation deposition with Sb powder as precursor. The rods, of rectangular cross section, are composed of weakly bonded stacks of tiny plates of few hundreds of nanometres, which self-assembled during the growth process parallel to the growth axis. Photoluminescence (PL) spectra show resonance peaks in the ultraviolet-blue region related to optical cavity modes across the cross sections of the rods. Local phase transformation from the orthorhombic to the cubic Sb_2O_3 phase has been induced by long irradiation with the 325 nm laser light, as confirmed by Raman spectroscopy and PL.

Keywords Antimony oxide · Luminescence · Phase transition

Introduction

Antimony trioxide Sb_2O_3 is a semiconductor oxide which has applications as flame retardant, UV filter, catalyst (Zhang et al. 2004) and optical devices (Li et al. 2011). Some potential applications of this material in optoelectronic devices have been related to its high refraction index as reported for Sb_2O_3 films (Sahoo and Apparao 1996). Also optical resonances associated with Fabry–Perot cavity modes and whispering gallery modes have been found in Sb_2O_3 microtriangles (Cebriano et al. 2012a) and antimony-based glasses, and nano-glass ceramics containing Sb_2O_3 have been proposed for optical applications (Som and Karmakar 2010). In addition, the development of organic–inorganic hybrid nanomaterials involving antimony oxide for biomedical sensing is attracting increasing interest. For example, Lu et al. 2006 have proposed that modified antimony oxide nanorods may be suitable as effective biocompatible sensing systems for redox proteins in medical applications. Sb_2O_3 exists as two crystalline phases, the cubic phase (Svensonn 1975) or senarmontite and the orthorhombic phase (Svensonn 1974) or valentinite. As in the case of other semiconductor oxides, nanostructured Sb_2O_3 has been also investigated with respect to nanotechnology applications and different orthorhombic nano- and microstructures have been reported. In particular, orthorhombic-elongated low-dimensional structures have been grown by solution routes (Deng et al. 2006, 2007, 2009; Naidu et al. 2009), by a surfactant-assisted solvothermal method (Zhang et al. 2004; Li et al. 2011) or by carbothermal reduction (Fan et al. 2011). Thermal evaporation deposition has been used to grow micro- and

Electronic supplementary material The online version of this article (doi:10.1007/s11051-013-1667-5) contains supplementary material, which is available to authorized users.

T. Cebriano · B. Méndez (✉) · J. Piqueras
Departamento de Física de Materiales, Facultad de Ciencias Físicas, Universidad Complutense de Madrid, 28040 Madrid, Spain
e-mail: bianchi@fis.ucm.es

nanostructures of the cubic phase such as nanoparticles (Hu et al. 2007), microspheres and nano- and microtriangles (Cebriano et al. 2012a, b). In spite of the relatively few works on Sb_2O_3 nanostructures as compared with other more investigated semiconducting oxides as for instance, ZnO, SnO_2 or TiO_2, there are several results regarding self-assembly processes in Sb_2O_3. It has been recently found that depending on the temperature Sb_2O_3 nanowires either axially self-assembled into multisegmented nanowires, or formed nanobelts by a side-by-side self-assembly process (Deng et al. 2007). Wang et al. 2011 have reported the orthorhombic nanowires assembling to form microspheres during hydrothermal growth. We have previously found that microspheres were formed by assembled nanoparticles of the cubic phase while nanotriangles self-assembled to form ordered arrays of microtriangles (Cebriano et al. 2012b). In this work, orthorhombic Sb_2O_3 micro- and nanorods have been grown by evaporation deposition. The rods are formed by assembled plates or belts, parallel to the growth axis as revealed by secondary electron observations and by irradiation experiments in the scanning electron microscope (SEM). Optical behaviour of the structures has been investigated by luminescence, including analysis of optical resonances, and Raman spectroscopy.

Experimental

A precursor formed by powder of metallic Sb was placed in an alumina boat in the centre of a tubular furnace and heated at 900 °C during 1 h under nitrogen flow. Since the furnace was not sealed for vacuum conditions, slow oxidation took place during the thermal treatment. In a colder area of the furnace, at 400 °C, in the opposite side of the gas inlet, a disc of a compacted mixture of Sb and SnO_2 powders, with 5 wt% of SnO_2, of about 1 cm diameter and 1 mm thickness, acted as source and as substrate for some of the structures grown during the treatment. At the same time, other structures were grown on the furnace tube wall where temperature was 550 °C. In a previous work (Cebriano et al. 2012b) the disc was formed only by compacted Sb powder and the structures grown on this substrate were Sb_2O_3 microspheres and microtriangles of the cubic phase. The addition of Sn to the precursor has been previously found to favour the growth by evaporation deposition of elongated, hierarchical and other complex small dimensional structures of different oxides such as ZnO (Ortega et al. 2009; 2011) GeO_2 (Hidalgo et al. 2008) or Ga_2O_3 (López et al. 2012). The addition of SnO_2 to the Sb metallic precursor in this work was aimed to induce the growth of elongated structures as in the mentioned references. X-ray diffraction (XRD) measurements were performed with an XPert Pro diffractometer. The morphology of the structures was characterized with either a Leica 440 or FEI Inspect scanning electron microscopes (SEM). Energy-dispersive spectroscopy (EDS) was performed with a Bruker AXS Quantax system in a Leica 440 SEM. For the analysis in the SEM of the crystal phase and the orientation of the faces of single structures an electron backscatter diffraction (EBSD) Bruker Quantax CrystAlign system was used. The EBSD patterns were acquired using an acceleration voltage of 25 kV. The specimen holder was tilted 70° towards the phosphor detector and the sample-phosphor distance was 20 mm. Raman and photoluminescence measurements were performed with a Horiba LabRam Hr800 confocal microscope with a 325 nm He–Cd laser.

Results and discussion

The thermal evaporation method used lead to the growth of arrays of ordered micro- and nanotriangles, octahedral crystallites and microrods on the Sb–SnO_2 substrate. The microtriangles appear only at the rim of the pellet (Fig. 1a) and are similar to those previously described for a pure Sb substrate (Cebriano et al. 2012b). EDS measurements on these triangles show a Sn content in the range of about 1.9–3 % for the Sn/Sb ratio. EBSD measurements on the triangles show that the exposed faces are (111) planes and confirm that they belong to the senarmontite or cubic phase (Fig. 1b). On the other hand, the surface of the pellet substrate is almost fully covered with faceted crystals of octahedral shape and rods with thicknesses from the submicron range to several microns and lengths up to 100 μm or more. Therefore, the presence of SnO_2 in the substrate seems to favour the growth of rods, which were not formed on pure Sb substrates. Figure 2a shows the distribution of rods and of dispersed larger faceted crystallites of octahedral shape on the substrate surface. It should be noticed that most of the rods

arise from the triangular faces of the octahedrons. Figure 2b shows an example of a rod, which is composed of smaller rods, or belt-shaped plates, stacked parallel to the rod axis evidencing a self-assembling process during the growth. Most of the rods have a pointed tip, as can be observed in the inset of Fig. 2a. X-ray microanalysis data of these structures reveal that their Sn content is somewhat lower, about 1 % for Sn/Sb ratio, than in the triangles and crystallites.

In addition, a large amount of rods was deposited on the inner wall of the furnace tube at a position of 550 °C temperature, with the source at 900 °C. The rods were detached from the tube and deposited on a graphite substrate for their study in the SEM. Similar to the rods grown on the Sb–SnO_2 substrate these rods

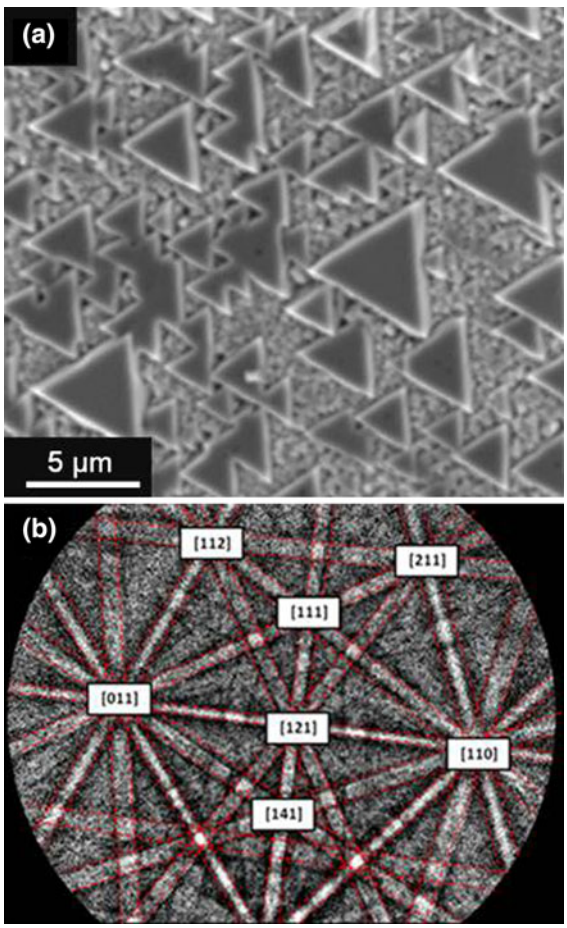

Fig. 1 **a** Representative SEM image of Sb_2O_3 microtriangles. **b** Kikuchi pattern recorded at the centre of one of the triangles with the symmetries of the cubic phase. The zone axis is the [111] direction

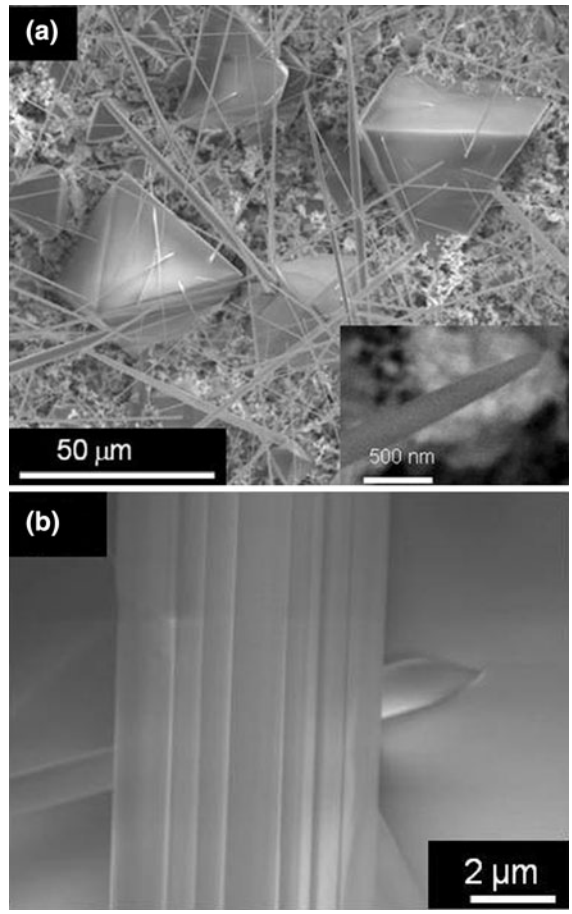

Fig. 2 **a** SEM image of structures grown on the antimony substrate. *Inset*: detail of the tip of a rod. **b** Detail of a rod composed of parallel plates

are composed by smaller plates stacked parallel to the growth axis (Fig. 3a). In some cases it is observed that the plates are stacked in different sets, all parallel to the axis but forming a complex array with stacks in different orientations. EBSD analysis shows that the rods belong to the orthorhombic phase of Sb_2O_3 and the faces of the large rods could be indexed as (100), (010) or (001) (Fig. 3b).

The lamellar structure of the rods is evidenced in the SEM, especially when high electron beam currents are used. SEM images corresponding to orthorhombic rods on a graphite substrate show that the top part of some rods has an enhanced signal (see supporting information). This contrast in the secondary electron images indicates the existence of charge effects, so that by high beam injection the charge injected in the top areas of the rods, which are far from the conductive

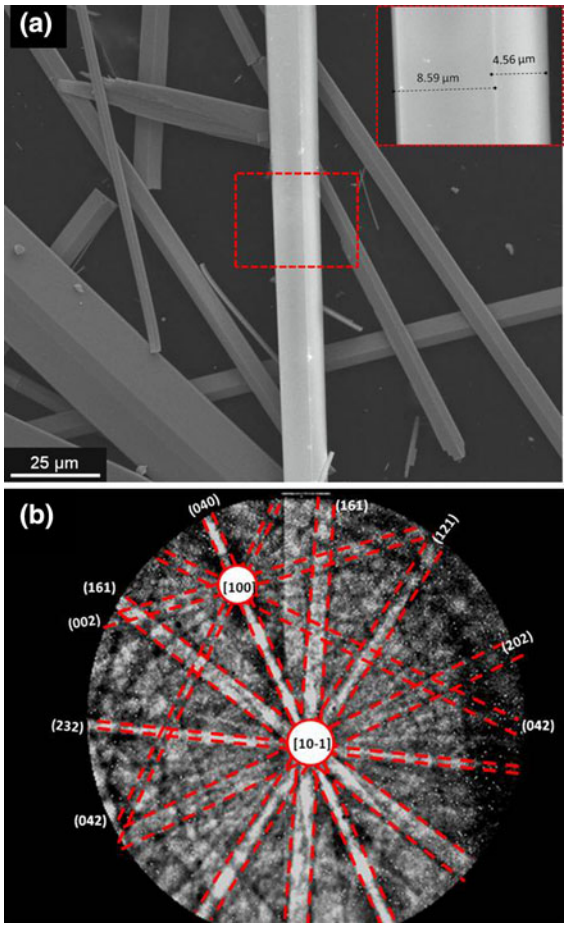

Fig. 3 **a** SEM image of rods deposited on the tube wall. *Inset*: detail of the *rod* highlighted by the *red square*. **b** Indexed EBSD Kikuchi patterns obtained from one of the rod *rectangular faces*. (color figure online)

substrate, do not dissipate so rapidly as those charges that are closer to the substrate. During observation in the SEM the rods are not static but as a consequence of the charge effects, some rods separate into two plates parallel to the growth axis which join again in a repetitive way, with a gripper-like motion, during the electron irradiation. This shows that the thin plates forming the rod, as those shown in Figs. 2 and 3, are independent structures that are only weakly attached, or self-assembled, during the rod growth process. The supporting information includes a video showing the motion of the components of the rods under SEM observation, and Fig. 4 shows two images in which motion of some rods is observed. The fact that the rods partially dissociate during electron injection and subsequently recover the original shape, suggest that the assembling of the plates is associated with electrostatic forces. Charge accumulation on a face of the rod exposed to the electron beam would break the electrostatic equilibrium and cause the repulsion between two parts of the rods and their separation. During scanning, the excess charge can dissipate and the rod recovers the original equilibrium. It is to be noticed that the separation takes place only along a length close to the top so that the rods do not totally split, which is explained by the reduced charging near the substrate. To our knowledge, rods formed by electrostatic interaction of thin slabs and their reversible electrically induced splitting have not been previously reported. Electrostatic interaction has been also found to cause bending and bundling of ZnO nanowires in SEM (Liu et al. 2008) but, contrary to the present work, electron beam bombardment was excluded as the origin of this interaction. On the other hand the attraction among Au/ZnO nanorods observed in SEM (Wang et al. 2005) has been explained by interaction between accumulated charges near metal–semiconductor junctions in the nanorods. The effects observed in this work under the electron beam have a different origin than those of the interaction among nanowires reported by Liu et al. (2008) and Wang et al. (2005) and appear to be related to the weakly bonded self-assembled stacks in the microrods. Charge fluctuations in [100] faces in the course of vapour deposition could induce the formation of rods composed by plates instead of single crystalline rods.

PL spectra of the microrods (Fig. 5) show a band at about 3.2 eV (387 nm) corresponding to the near band edge emission of the orthorhombic phase (Zhang et al. 2004; Deng et al. 2006), a shoulder at about 3 eV (413 nm) and a broad band at lower energies, 1.9–2.5 eV, (500–650 nm), which have been suggested to be due to defect levels in the band gap associated with oxygen vacancies or surface defects (Naidu et al. 2009). The Fig. 5a shows a series of spectra recorded under different excitation conditions using absorption filters in the path of the excitation beam. By increasing the excitation density a red shift of the near band edge emission is observed as shown in Fig. 5b. This effect is related to sample heating by the laser beam which causes a reduction of the band gap and hence a band edge emission at lower energies. The sample temperature under different excitation densities could not be measured so that the evolution of the band gap cannot be quantitatively related to specific

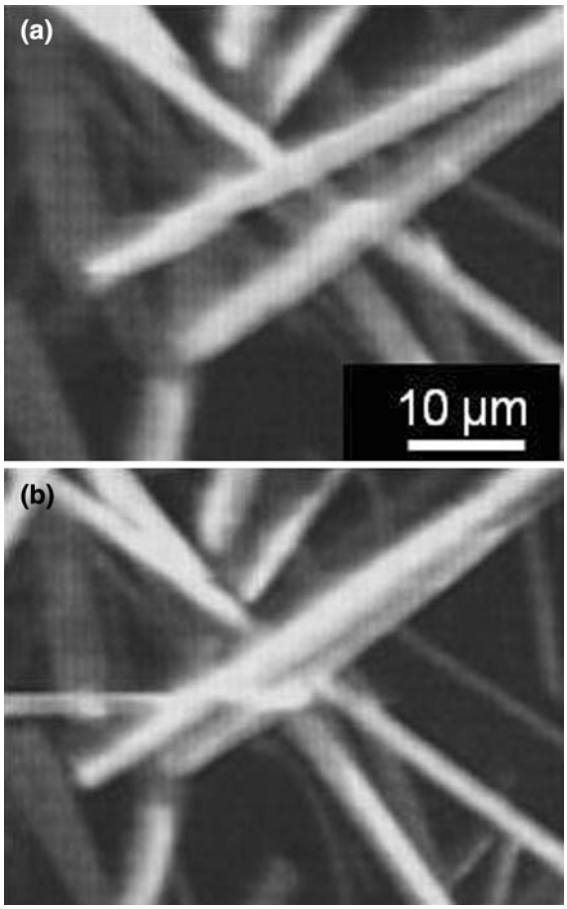

Fig. 4 Images from the video provided in the supplementary information. Partial splitting of the plates during irradiation is observed

temperature values. However, local heating with 325 nm illumination can involve significant temperature increase. For instance a phase transition which takes place in Bi_2O_3 above 700 °C was induced during observation with the same confocal laser microscope used in this work (Vila et al. 2012). Thermal phase transitions in antimony oxides have been recently studied and a transition temperature of orthorhombic into cubic phase of 615 °C was reported (Jones et al. 1987; Ormand and Holland 2007). This temperature can be exceeded under prolonged time exposure and high excitation conditions of the laser beam in the confocal microscope. We have carried out a study of both Raman and PL spectra as a function of irradiation time and marked changes have been observed, which reveal the orthorhombic to cubic phase transition. Figure 6 (lower spectrum) shows a Raman spectrum of the rods that corresponds to the orthorhombic Sb_2O_3 phase (Deng et al. 2006, 2009) with an intense peak at about 290 cm^{-1} and peaks at about 150, 193, 223, 508 and 600 cm^{-1}. After 100 min, the spectrum shows a main peak at 252 cm^{-1} while the initial dominant peak at 290 cm^{-1} has been quenched (Fig. 6). The 252 cm^{-1} Raman peak is the Sb–O–Sb stretching (A_1 type) of the molecular vibrations of the Sb_4O_6 rings in the cubic Sb_2O_3 structure. The final spectrum has been reported to correspond to the cubic phase of Sb_2O_3 (Cebriano et al. 2012b; Zeng et al. 2004). Therefore, the time evolution of the Raman spectra shows a laser-induced orthorhombic to cubic phase change. The existence of the phase transformation is supported by the corresponding evolution of the PL spectra during laser irradiation, shown in Fig. 7. The initial PL

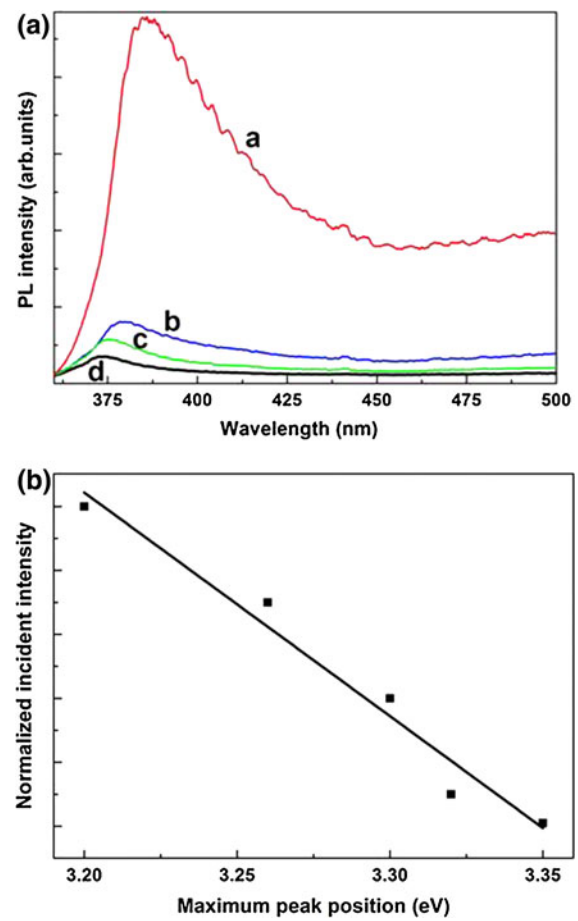

Fig. 5 **a** PL spectra of rods under different excitation densities. Curves labelled as *a*, *b*, *c* and *d* stand for laser input intensities of I_0, $I_0 10^{-0.3}$, $I_0 10^{-0.6}$ and $I_0 10^{-1}$, respectively. **b** Dependence of the maximum peak position with the excitation energy

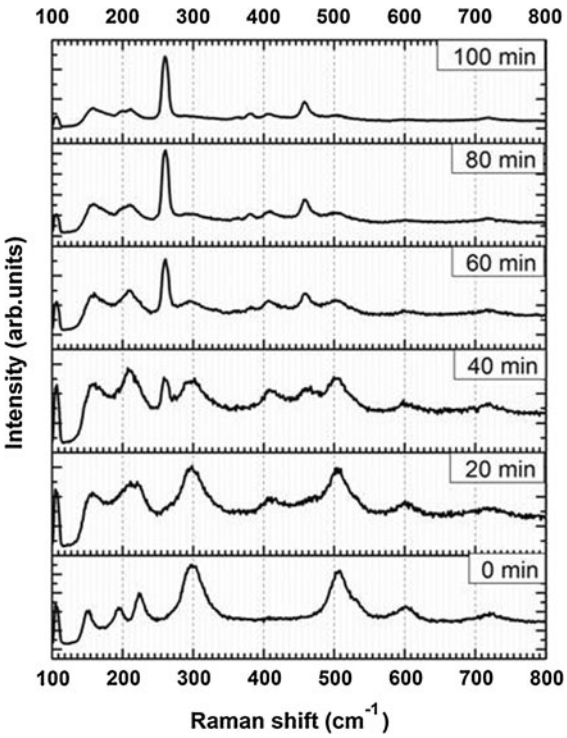

Fig. 6 Evolution of Raman spectra of the orthorhombic rods as a function of the irradiation time

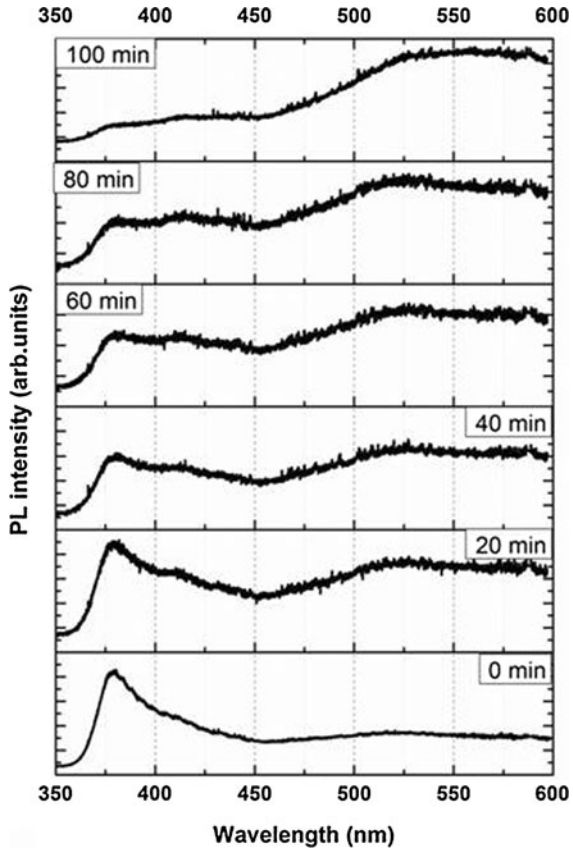

Fig. 7 Evolution of PL spectra of the orthorhombic rods as a function of the irradiation time

spectrum shows the near band edge emission of the orthorhombic structure at about 3.2 eV. This band is quenched after the 100 min irradiation as a consequence of the phase transformation. Since the reported band gap in Sb_2O_3 films of the cubic phase is in the range 3.71–3.98 eV, band gap transitions are probably not excited with the laser used in this work, so that the band edge emission is absent in the final spectrum as in the previously reported spectra of cubic Sb_2O_3 microstructures (Cebriano et al. 2012b).

Under high laser excitation, series of resonance peaks are observed in the PL spectra of the rods as shown in the spectrum (a) of Fig. 5a. The possibility that these resonance peaks are related to a Fabry–Perot (FP) cavity modes has been investigated by measuring the separation of the resonance peaks in rods with different lengths and widths according to the expression $\Delta\lambda = \lambda^2/2Ln$, where $\Delta\lambda$ is the peaks separation, L the cavity length and n the refraction index. The measured $\Delta\lambda$ separations correspond to cavity lengths in the range from few microns up to about 10 μ, by considering a refractive index of 2.1 (Tigau et al. 2005). Since the lengths of the measured rods were typically of about hundred microns, the possibility that the resonances are generated by propagation along the longitudinal dimension of the rod can be excluded. Figure 3a shows the SEM image of one of the resonant rods with a rectangular cross section of 8.1 μm (width) by 4.5 μm (height). The PL spectrum recorded at the upper face is shown in Fig. 8a, which clearly reveals resonant peaks. The cavity size is estimated according to the Fabry–Perot rule and results of 8.06 μm, in good agreement with the rod width, w. FP resonances have been observed in several rods of different sizes and $\Delta\lambda$ values were measured at a fixed wavelength from the PL spectra. By plotting $\Delta\lambda$ versus the inverse of the cavity length, $1/w$, for ten rods (Fig. 8b) a fitting line can be drawn. From the slope of the line, a group refractive index of 2.15 is obtained, which is in accordance with the refraction index reported by optical transmission in thin films (Tigau et al. 2005). The high crystalline quality and the smooth surfaces of

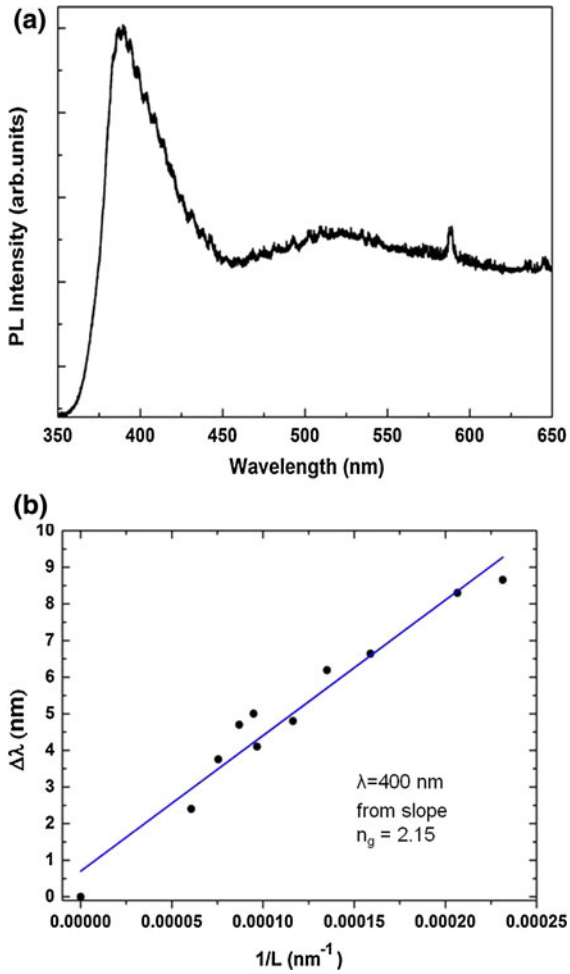

Fig. 8 **a** PL spectrum of the *rod* shown in Fig. 3a. **b** Resonance peak separation, $\Delta\lambda$, versus the inverse of the *rod* size, $1/w$, measured from ten different *rods* and the linear fitting to the Fabry–Perot law

Sb_2O_3 microrods enable the observation of FP resonant modes, which could be useful for their applications as optical cavities in the ultraviolet-blue region.

Conclusions

Sn-doped Sb_2O_3 microtriangles of the cubic phase as well as microrods of the orthorhombic phase have been grown by a thermal evaporation method with a mixture of SnO_2 and metallic Sb as precursor. The microrods, with rectangular shaped cross section, are formed by several rectangular plates of submicron sizes, which are self-assembled parallel to the growth axis during the growth. The plates are weakly bonded and charge accumulation during observation in SEM induces their partial separation with a gripper-like motion. PL spectra of the microrods show band gap emission at about 3.2 eV and defects bands at lower energies. An orthorhombic to cubic local phase transformation induced by laser irradiation is revealed by changes in the PL and Raman spectra. Resonance peaks in the PL spectra are related to Fabry–Perot cavity modes across the width of the rods.

Acknowledgments This study has been supported by Spanish MICINN through projects MAT 2009-07882, MAT 2012-31959 and Consolider 2010-00013.

References

Cebriano T, Méndez B, Piqueras J (2012a) Study of luminescence and optical resonances in Sb_2O_3 micro- and nanotriangles. J Nanopart Res 14:1215

Cebriano T, Méndez B, Piqueras J (2012b) Micro- and nanostructures of Sb_2O_3 grown by evaporation deposition: self assembly phenomena, fractal and dendritic growth. Mat. Chem. Phys. 135:1096–1103

Deng Z, Tang F, Chen D, Meng X, Cao L, Zou B (2006) A simple solution route to single-crystalline Sb_2O_3 nanowires with rectangular cross sections. J Phys Chem B 110: 18225–18230

Deng Z, Chen D, Tang F, Meng X, Ren J, Zhang L (2007) Orientated attachment assisted self-assembly of Sb_2O_3 nanorods and nanowires: end-to-end versus side-by-side. J Phys Chem C 111:5325–5330

Deng Z, Chen D, Tang F, Ren J, Muscat AJ (2009) Synthesis and purple-blue emission of antimony trioxide single-crystalline nanobelts with elliptical cross section. Nano Res 2:151–160

Fan G, Huang Z, Chai C, Liao D (2011) Synthesis of micro-sized Sb_2O_3 hierarchical structures by carbothermal reduction method. Mat Lett 65:1141–1144

Hidalgo P, Méndez B, Piqueras J (2008) Sn doped GeO_2 nanowires with waveguiding behavior. Nanotechnology 19:455705

Hu CH, Shi SQ, Surya C, Woo CH (2007) Synthesis of antimony oxide nano-particles by vapor transport and condensation. J Mater Sci 42:9855–9858

Jones SA, Fenerty J, Pearce J (1987) The enantiotropic phase transition of antimony (III) oxide. Thermochim Acta 114:61–66

Li L, Zhang YX, Fang XS, Zhai TY, Liao MY, Wang HQ, Li GH, Koide Y, Bando Y, Goldberg D (2011) Sb_2O_3 nanobelt networks for excellent visible-light-range photodetectors. Nanotechnology 22:165704

Liu J, Lee S, Lee K, Ahn YH, Park JY, Koh KH (2008) Bending and bundling of metal-free vertically aligned ZnO nanowires due to electrostatic interaction. Nanotechnology 19:186607

López I, Nogales E, Méndez B, Piqueras J (2012) Resonant cavity modes in gallium oxide microwires. Appl Phys Lett 100:261910

Lu X, Wen Z, Li J (2006) Hydroxyl-containing antimony oxide bromide nanorods combined with chitosan for biosensors. Biomaterials 27:5740–5747

Naidu BS, Pandey M, Sudarsan V, Vatsa RK, Tewari R (2009) Photoluminescence and Raman spectroscopic investigations of morphology assisted effects in Sb_2O_3. Chem Phys Lett 474:180–184

Ormand RG, Holland D (2007) Thermal phase transitions in antimony (III) oxides. J Sol State Chem 180:2587–2596

Ortega Y, Fernández P, Piqueras J (2009) Self-assembled tin-doped ZnO nanowire and nanoplate structures grown by thermal treatment of ZnS powder. J Cryst Growth 311:3231–3234

Ortega Y, Fernández P, Piqueras J (2011) Self-assembled three-dimensional Al-doped ZnO nanorod networks. Semicond Sci Technol 26:085035

Sahoo NK, Apparao KVSR (1996) Process-parameter optimization of Sb_2O_3 films in the ultraviolet and visible region for interferometric applications. Appl Phys A 63:195–202

Som T, Karmakar B (2010) Structure and properties of low-phonon antimony glasses and nano glass-ceramics in K_2O–B_2O_3–Sb_2O_3 system. J Non-Cryst Solids 356:987–999

Svensonn C (1974) The crystal structure of orthorhombic antimony trioxide, Sb_2O_3. Acta Cryst B 30:458–461

Svensonn C (1975) Refinement of the crystal structure of cubic antimony trioxide, Sb_2O_3. Acta Cryst B 31:2016–2018

Tigau N, Ciupina V, Prodan G (2005) The effect of substrate temperature on the optical properties of polycrystalline Sb_2O_3 thin films. J Cryst Growth 277:529–535

Vila M, Díaz-Guerra C, Piqueras J (2012) Laser irradiation-induced α to δ phase transformation in Bi_2O_3 ceramics and nanowires. Appl Phys Lett 101:071905

Wang X, Summers CJ, Wang ZL (2005) Self-attraction among aligned Au/ZnO nanorods under electron beam. Appl Phys Lett 86:013111

Wang Q, Ge S, Shao Q, Zhao Y (2011) Self-assembly of Sb_2O_3 nanowires into microspheres: synthesis and characterization. Phys B 406:731–736

Zeng DW, Xie CS, Zhu BL, Song WL (2004) Characteristics of Sb_2O_3 nanoparticles synthesized from antimony by vapor condensation method. Mat Lett 58:312–315

Zhang Y, Li G, Zhang J, Zhang L (2004) Shape-controlled growth of one-dimensional Sb_2O_3 nanomaterials. Nanotechnology 15:762–765